Molecular basis for the R-type anion channel QUAC1 activity in guard cells

Li Qin[1,2#], Ling-hui Tang[1,2#], Jia-shu Xu[3,4#], Xian-hui Zhang[1,2#], Yun Zhu[3,4#], Chun-rui Zhang[1,2], Xue-lei Liu[1,2], Mei-hua Wang[1,2], Fei Li[5], Fei Sun[3,4], Min Su[1,2*], Yu-jia Zhai[3,4*] & Yu-hang Chen[1,2*]

[1] State Key Laboratory of Molecular Developmental Biology, Institute of Genetics and Developmental Biology, Chinese Academy of Sciences, Beijing, China; Innovative Academy of Seed Design, Chinese Academy of Sciences, Beijing 100101, China

[2] College of Advanced Agricultural Sciences, University of Chinese Academy of Sciences, Beijing 100049, China

[3] National Laboratory of Biomacromolecules, CAS Center for Excellence in Biomacromolecules, Institute of Biophysics, Chinese Academy of Sciences, Beijing 100101, China

[4] School of Life Sciences, University of Chinese Academy of Sciences, Beijing 100049, China

[5] Department of Biology, New York University, New York, NY 10003, USA

[#]These authors contributed equally to this work.

[*]Correspondence to:

Yu-hang Chen, E-mail: yuhang.chen@genetics.ac.cn; or

Yu-jia Zhai, E-mail: yujia@ibp.ac.cn; or

Min Su, E-mail: minsu@genetics.ac.cn.

SUMMARY

The rapid (R)-type anion channel plays a central role in controlling stomatal closure in plant guard cells, thus regulating the exchange of water and photosynthetic gas (CO_2) in response to environmental stimuli. The activity of the R- type anion channel is regulated by malate. However, the molecular basis of the R-type anion channel activity remains elusive. Here, we describe the first cryo-EM structure of the R-type anion channel QUAC1 at 3.5 Å resolution in the presence of malate. The structure reveals that the QUAC1 is a symmetrical dimer, forming a single electropositive T-shaped pore for passing anions across the membrane. The transmembrane and cytoplasmic domains are assembled into a twisted bi-layer architecture, with the associated dimeric interfaces nearly perpendicular. Our structural and functional analyses reveal that QUAC1 functions as an inward rectifying anion channel and suggests a mechanism for malate-mediated channel activation. Altogether, our study uncovers the molecular basis for a novel class of anion channels and provides insights into the gating and modulation of the R-type anion channel.

KEYWORDS

Guard cell, QUAC1, Channel, Cryo-EM, Electrophysiology

54   **INTRODUCTION**

55   Stomatal pore, formed by a pair of guard cells in leaf epidermis, plays a crucial role in regulating

56   CO_2 assimilation and water evaporation in plants [1,2]. Guard cells can integrate a wide range of

57   environmental stimuli, such as drought, humidity, high CO_2, and ozone, and convert them into

58   appropriate turgor pressure changes that regulate stomatal opening or closure [3,4].

59   It is well-established that anion effluxes are key events to initiate stomatal closure in

60   response to environmental stimuli [5–8]. Previous studies showed that the guard cells harbour two

61   distinct types of anion channels: rapid (R)-type and slow (S)-type [9–12]. The R-type anion channel

62   can be fully activated and rapidly inactivated within milliseconds, whereas the S-type anion

63   channel takes up to several tens of seconds to be activated, followed by slow inactivation

64   kinetics [10]. Recent works of <u>SL</u>ow <u>A</u>nion <u>C</u>hannel 1 (SLAC1), an S-type anion channel

65   discovered in *Arabidopsis* [13–15], have uncovered detailed mechanisms underlying S-type anion

66   channel activity [16–21]. However, the molecular basis of the biological role of the R-type anion

67   channel is still largely enigmatic due to the lack of structural information.

68   <u>QU</u>ick <u>A</u>nion <u>C</u>hannel 1 (QUAC1), initially named aluminium-activated malate

69   transporter12 (ALMT12), represents a guard cell R-type anion channel in *Arabidopsis* [22]. The

70   loss-of-function of *quac1* (*almt12*) mutation resulted in impaired stomatal closure [22,23]. A

71   double mutant lacking SLAC1 and QUAC1 was nearly unresponsive to various stimuli that

72   were expected to cause stomatal closure [24]. Apart from its role in stomatal regulation, QUAC1

73   also plays a vital role in cell polarity and the growth of pollen tubes via regulation of apical

74   anion efflux [25,26]. The activity of QUAC1 was reported to be modulated by malate [22,27–29], OST1

75   phosphorylation [30] and calmodulin [31], but the underlying mechanisms remain elusive.

76   Here, we report the first cryo-EM structure of soybean QUAC1 from Glycine max

77   (*Gm*QUAC1, ~67% sequence identity to Arabidopsis *At*QUAC1) at the resolution of 3.5 Å in

78   the presence of malate. The structure revealed that the QUAC1 is a symmetrical dimer

79   assembled into twisted bi-layer architecture with a central T-shaped pore across the membrane.

80   The pore is lined with highly conserved positively charged residues, rendering the pore surface

81   electropositive, consistent with the QUAC1 function as an anion channel. Further

3

82   electrophysiological analyses reveal that the QUAC1 displays rapid kinetics in channel gating

83   during activation and inactivation.

84   Our truncation study reveals that the N-terminal juxtamembrane helix is crucial in

85   maintaining structural integrity for proper channel function. Further mutagenesis analyses

86   demonstrate that the C-terminal interaction locks the channel in a high-energy state, and that a

87   domain-swapped helix plays an inhibitory role in channel regulation. Two pore-lining W90

88   residues, close to the lateral fenestration within the transmembrane domain, serve as toggle

89   switches to regulate gating during channel activation. Therefore, the unique architecture

90   endows QUAC1 function as an R-type anion channel, and our structural and functional analyses

91   allow us to propose a novel mechanism for malate-mediated channel activation. Altogether, our

92   study uncovers the molecular basis for a novel class of anion channels and provides insights

93   into the gating and modulation of the R-type anion channel.

94

95   **RESULTS**

96   **Bioinformatics analyses of plant ALMTs/QUACs**

97   QUAC1 belongs to the ALMT family, which has diverse functions in plants, including stomatal

98   function [22,23,32–34], pollen tube growth [25,26], Al^{3+} resistance [35–38], mineral nutrition [39,40], fruit

99   acidity [41,42], microbe interactions [43,44], and seed development [45,46]. There are thirteen members

100   in the model plant *Arabidopsis thaliana*, except for one short sequence of a partial

101   transmembrane domain (ALMT11). To better understand how QUAC (ALMT) proteins are

102   represented in the plant kingdom, we clustered ~1,700 non-redundant sequences into a

103   superfamily at the PSI-BLAST level $E \leq 5 \times 10^{-3}$, then into two distinct families at a threshold of

104    $E \leq 10^{-160}$, and finally into subfamilies at a threshold of $E \leq 10^{-180}$, as detailed in Extended Data

105   Table 1.

106   Since more studies have shown that ALMT members function as anion channels rather

107   than transporters, and the QUAC1 is now the best-characterized member, we adopted

108   nomenclature for the QUAC superfamily, which was further divided into families QF1 and QF2.

109   We further found that family QF1 has two subfamilies: QF1A comprises the *Arabidopsis*

110   ALMT3, 4, 5, 6, 9 and their homologs, and QF1B has a distinct set of ALMT proteins. Family

4

111 QF2 has three subfamilies: the *Arabidopsis* ALMT1, 2, 7, 8, 10 proteins are in subfamily QF2A,

112 the *Arabidopsis* ALMT12, 13, 14 proteins are in QF2B, and another distinct set of ALMT

113 proteins are in QF2C (Extended Data Fig. 1).

114 The structure-based sequence alignment for the *Gm*QUAC1 and thirteen *Arabidopsis*

115 QUAC/ALMTs is shown in Extended Data Fig. 2. Sequence analyses reveal that the ALMTs

116 share relatively conserved transmembrane and cytosolic helical regions. Some conserved

117 positively charged residues are distributed in the transmembrane regions and may be

118 responsible for anion selectivity or voltage sensing. Some fingerprint motifs, including WEP

119 (Trp-Glu-Pro) and PXWXG (Pro-X-Trp-X-Gly), are found in the cytosolic helical region. One

120 of the most divergent regions (~50-100 aa in length) is found between H5 and H6 helices in the

121 cytosolic portions, harbouring potential phosphorylation residues (Ser/Thr) for channel

122 modulation. Further studies will provide mechanistic insight into the regulation of these

123 characteristic motifs or distinct sets of QUACs.

124

125 **Cryo-EM structural determination of QUAC1**

126 We screened six plant QUAC1s for expression and found that the *Gm*QUAC1 was suitable for

127 further structural and functional studies (see method for details). Upon solubilization in 1.0%

128 n-dodecyl-β-D-maltopyranoside (DDM) and 0.02% cholesteryl hemisuccinate (CHS), the

129 *Gm*QUAC1 proteins were purified by Ni^{2+}-affinity chromatography, and the resulting peak-

130 fractions were pooled and loaded onto a gel-filtration column for further purification, buffer

131 and detergent exchange. The final solution contained 0.005% detergent LMNG, with either 150

132 mM NaCl or 75 mM L-malate.

133 We further determined its cryo-EM structure in the presence of 75 mM L-malate

134 (Extended Data Fig. 3, 4 and Extended Data Table 2). The dimeric reconstruction at 3.5 Å

135 resolution allowed *de novo* modelling of 410 of the 537 amino acids (residues 36-393 and 455-

136 506) per protomer chain. Other regions are not resolved in the density map due to their intrinsic

137 flexibility in the protein. The search in the Dali server [47] for similar structures returned no

138 significant hit. To the best of our knowledge, the QUAC1 protomer has a unique protein fold

139 and architecture, representing a novel class of ion channels.

5

140

The QUAC1 channel forms a twisted bi-layer architecture

141

142 The QUAC1 channel is a flat vase-shaped homodimer with a two-fold axis perpendicular to the

143 plasma membrane (Fig. 1a and Supplementary Video 1). The overall molecule forms a bi-layer

144 architecture, divided into two portions of the transmembrane domain (TMD) and the

145 cytoplasmic helical domain (CHD). The domain topology for each protomer is shown in Fig.

146 1b. The TMD comprises 6 TM helices, arranging as three pairs of V-shaped helical hairpins

147 stacked against each other, whereas the CHD has 7 helices, forming a helical bundle with a

148 short domain-swapped finger helix. The N-terminal pre-TM region contains a juxtamembrane

149 helix bent at a conserved proline before the TMD. A disorder region between helix H5 and H6

150 in the CHD enriches with Ser/Thr residues (Extended Data Fig. 2), raising an intriguing

151 possibility of containing phosphorylation sites for channel regulation.

152 The dimer formation is mediated by interactions from both TMDs and CHDs, which bury

153 surface areas of ~3,500 $Å^2$ and ~3,300 $Å^2$, respectively. When viewed from the extracellular

154 side, the TM helices trace the circumference of an ellipse with TM1-TM6 from one protomer

155 followed by another set of TM1-TM6 from the second protomer in an antiparallel manner (Fig.

156 1c). At the membrane, TM1 and TM2 directly interact with TM4 and TM5 from another

157 protomer, respectively. In the cytoplasm, the CHD of each protomer unites together at the distal

158 end of the molecule, mediated by intensive interactions. A domain-swapped finger helix (H6)

159 also participates in C-terminal interactions (Fig. 1d). However, the functional role of these

160 interactions remains unclear.

161 In the bi-layer structure of QUAC1, the TMDs connect to the CHDs via a highly conserved

162 PXWXG motif (Pro-X-Trp-X-Gly). They interact with each other in a twisted manner, with

163 their dimeric interfaces nearly perpendicular to each other (forming a dihedral angle of ~83º)

164 (Fig. 2a). Interestingly, another characteristic motif WEP (Trp-Glu-Pro), located in the

165 connecting loop between helix H2 and H3, is found in the vicinity of the PXWXG motif at the

166 layer interface between TMD and CHD. These two motifs, together with other surrounding

167 charged residues (Arg/Lys: R56, K63, R291, and R294; Asp/Glu: D54, E223, D224, and E289),

6

168 form intensive interactions at the layer interface, and thus may play a vital role in coupling

169 channel regulation to gating (Fig. 2b). Mutations in the WEP motif (E286Q in *Ta*ALMT1 and

170 E276Q in *At*QUAC1) [27,48] completely abolish their channel activities, possibly due to impaired

171 coupling between the TMD and CHD caused by the altered interaction at the layer interface.

172 Thus, the unique architecture design causes the channel in a high-energy state, providing a

173 structural basis for QUAC1 function as an R-type channel. These observations also imply that

174 the intramolecular domain rearrangements may occur upon channel activation.

175

176 **Structural features of the ion conduction pathway in QUAC1**

177 Unlike the trimeric SLAC1, which has three independent pores [20], the dimeric QUAC1 forms

178 a single T-shaped tunnel with a bifurcated entrance in the cytoplasm (Fig. 3a). The TM2, TM3,

179 TM5, and TM6 from both protomers create a pore with a radius of ~4-6 Å within the membrane

180 (Fig. 3b), as estimated by HOLE [49]. Overall, the QUAC1 pore is lined with highly conserved

181 and general hydrophobic residues (Fig. 3c). Nevertheless, some highly conserved positively

182 charged residues are distributed along the pore, thus rendering the surface electropositive (Fig.

183 3d).

184 Two arginines (R187 and R198) form a positively charged ring facing the pore entrance

185 at the extracellular side. Three positively charged residues from TM3 and TM4 (K109, R113,

186 and R158) protrude into the pore, making a second positively charged ring within the membrane.

187 They are associated with other conserved residues from TM2 and TM5 (E100, D168, and Y169),

188 mediating an inter-helices network within the pore. Another two lysines (K164 and K165) form

189 additional constrictions at the bottom of the T-shaped pore (Fig. 3e). Altogether, the structural

190 feature of QUAC1 likely contributes to its function as an anion-conducting channel. The above

191 findings suggest that permeable anions interact with the pore-lining charged residues, thus

192 participating in channel regulation.

193 Remarkably, a central kink (~24º) in TM6 causes a lateral fenestration from the membrane

194 to the lumen of the channel pore within each protomer (Fig. 4a). The fenestration measures ~6

195 Å × 20 Å, and its dimension depends upon the conformation of pore-forming TMs, especially

196 the kinked TM6. The presence of kinked helix and lateral fenestration in the structure implies

197 that the channel in 75 mM malate is in a constrained conformation. Interestingly, several

198 unmodeled densities and a highly conserved pore-lining W90 residue are found within or near

199 the fenestration (Fig. 4b), raising an interesting question if the bulky W90 residue serves as a

200 toggle switch to regulate channel gating during QUAC1 activation.

201

202 **Functional characterization of QUAC1 by TEVC**

203 A total of 34 ALMTs were found in soybean [50], but none of them has yet been functionally

204 characterized by electrophysiology. We expressed the *Gm*QUAC1/ALMT12 in *Xenopus laevis*

205 oocytes and measured channel conductance by applying the two-electrode voltage-clamp

206 (TEVC) technique. In the recordings, the application of voltage pulses elicited rapidly

207 activating currents in the bath solution of malate, resembling the *At*QUAC1 [22]. We also found

208 that the steady-state currents mediated by *Gm*QUAC1 displayed a bell-shaped current-voltage

209 curve (Extended Data Fig. 5). This electrophysiological behaviour points to a strong voltage

210 dependence for the QUAC1 channel activation, a hallmark feature of the R-type anion channel

211 in guard cells [10,22].

212 We also measured the conductance of *Gm*QUAC1 in other bath solutions. Surprisingly,

213 we found that the activation/inactivation kinetics and voltage-dependency of *Gm*QUAC1 in

214 $NaNO_3$ or NaCl solutions are distinguished from those in malate solution (Extended Data Fig.

215 5). In contrast to substantial instantaneous currents, only small steady-state currents can be seen

216 in the recording of *Gm*QUAC1 in the bath solution of $NaNO_3$ or NaCl (Extended Data Fig. 5).

217 Overall, our TEVC recordings demonstrate that external anions play a crucial role in regulating

218 QUAC1 channel properties, especially the activation/inactivation kinetics and steady-state

219 currents. We hypothesize that the anions interplay with the pore-lining residues, such as the

220 inter-helices charged residues interacting network within the pore (Fig. 3e), and act as door

221 stopper wedges to regulate channel gating.

222

223

8

Single-channel analysis of QUAC1 channel in planar lipid bilayer

To further understand the single-channel properties, we first fused the *Gm*QUAC1^{NaCl} proteins (purified in 150 mM NaCl) into a lipid bilayer and measured channel conductance under different symmetrical solutions (Fig. 5a). When using symmetrical NaNO$_3$ solutions, the application of a series of transmembrane voltages to the *trans* chamber resulted in frequent openings and closings of the *Gm*QUAC1 channel, as evidenced by the current fluctuation in the recording traces at different applied voltages (Extended Data Fig. 6a). We also found that the channel gating transits between two predominant full open and closed states, and sometimes to a sub-conductance that is ~50% level of the full conductance (Fig. 5b). This observation is consistent with the two-entrance T-shaped tunnel presented in the QUAC1 channel (Fig. 3a). At ~50% of the full level, the intermediate sub-conductance suggested one of two entrances was blocked or closed. In addition, the QUAC1 channel gating displays a flickering feature that represents the rapid character of the activation/inaction kinetics for R-type anion channels.

In contrast, we observed much reduced channel activity in the measurements in the solution of 150 mM NaCl (Extended Data Fig. 6b). The mean single-channel conductance for the *Gm*QUAC1^{NaCl} is 75.5 ± 4.5 pS (n=5) and 58.5 ± 7.0 pS (n=5) in the solutions of NaNO$_3$ and NaCl, respectively (Fig. 5c). Intriguingly, the channel open probability displays a strong voltage dependency, much higher at positive voltage than at negative one (Fig. 5d). As in our experimental setup, positive currents mean anions flow from the *cis* (representing cytoplasm) to the *trans*-chamber (representing extracellular side), and *vice versa*. Therefore, these results demonstrate that the QUAC1 channel functions as an R-type anion channel, favouring efflux (corresponding to anions flow from *cis*- to *trans*-chamber).

Malate regulates QUAC1 channel gating.

To investigate the effect of malate on the channel activity, we reproduced the same experiments with the *Gm*QUAC1^{malate} (purified in 75 mM L-malate) as above. Interestingly, we observed that *Gm*QUAC1^{malate} exhibits a similar current amplitude but a much higher open probability than those with *Gm*QUAC1^{NaCl} in both solutions of NaNO$_3$ and NaCl (Fig. 5c and Extended

9

252   Data Fig. 6). The mean single-channel conductance for the GmQUAC1^{malate} is 88.5 ± 2.4 pS

253   (n=4) and 62.7 ± 4.1 pS (n=4) in the solutions of NaNO$_3$ and NaCl, respectively. The open

254   probabilities of GmQUAC1^{malate} also display a similar voltage dependency as observed for

255   GmQUAC1^{NaCl} (Figure 5D and S6). Taken together, our results suggest that malate regulates

256   QUAC1 activation by modulating channel opening probability.

257   To further examine malate regulation on the channel gating, 2 mM L-malate was added to

258   the solutions upon the GmQUAC1^{NaCl} fused into a lipid bilayer. Interestingly, the channels

259   became more active after adding 2 mM L-malate to either the *trans*- or *cis*-chamber (Fig. 6a

260   and 6b). The current amplitude slightly increases, whereas the open probability becomes much

261   higher (Fig. 6c and 6d). These observations confirm that malate can stimulate channel activity

262   via enhanced open probability. Our findings also suggest that the malate regulation site may be

263   located within the pore and can be accessed from either the extracellular or intracellular side of

264   the membrane. We speculate that the GmQUAC1 structure in the presence of 75 mM L-malate

265   may represent an open state, although the malate-binding site remained unclear due to

266   insufficient information.

267

268   **The N-terminal pre-TM helix is required for channel activity.**

269   The sequence analysis shows that the N-terminal segment before TMD is one of the most

270   divergent regions in the QUAC family (Extended Data Fig. 2). The QUAC1 structure reveals

271   that this region contains a juxtamembrane pre-TM helix (Fig. 1b), enriching positively charged

272   residues. To examine its functional role, we designed a truncation construct (Δ1-53).

273   Surprisingly, we found that the Δ1-53 mutant resulted in nearly null currents in the TEVC

274   recordings (Extended Data Fig. 7). The observation demonstrates that the pre-TM helix is

275   indispensable for channel activity. Considering its association with the inner leaflet of the

276   membrane, we propose that the pre-TM helix may serve as a lever to regulate the proper

277   conformation of the QUAC1 channel.

278

279

The C-terminal dimeric interaction is crucial for channel function.

The cytosolic C-terminal portion is mainly formed by α-helices, except that a large divergent region between helix H5 and H6 is disordered or missing in the QUAC family (Extended Data Fig. 2). The *Gm*QUAC1 structure revealed extensive interactions between two CHDs at the distal end of the dimer (Fig. 7a). Two highly conserved hydrophobic residues (F470 and L474 from helix H7) protrude into the hydrophobic pocket formed by another protomer. Together with their antiparallel counterparts from another protomer, these bulky hydrophobic residues form a zipper-like interaction at the dimeric interface (Fig. 7b). In addition, a short finger helix (H6), whose sequence is conserved in the subfamily QF2B (Extended Data Fig. 2), also participates in the dimeric interaction in a domain-swapped manner (Fig. 7c). These interactions unite the two CHDs together and thus creates an anchor point for mechanical force transduction between TMD and CHD.

To investigate the functional role of the dimeric interactions in channel regulation, we generated mutations, aiming to disrupt the dimer-interface (A477E and F470A/L474A), or to break the finger helix interaction in H6 (Δ460-467 and S461D), in both the CHD (residues 221-537) bacteria-expression constructs for gel-filtration analysis and the full-length oocyte-expression constructs for conductance measurement. In contrast to the wild type, both dimer-interface disrupting mutants exhibited backwards-shifted elution peaks (from 9.2 ml to 10.2 ml) in the gel filtration profile and showed almost null currents in TEVC recording. In another experiment, the two altered helix H6 mutants cause loosened dimers but unexpectedly enhanced channel activities (Fig. 7d-f and Extended Data Fig. 8). Altogether, our results show that the C-terminal interaction has two important functions: (1) joins the two CHD together and locks the channel in a high-energy state; (2) a domain-swapped helix (H6) plays an inhibitory role, and its release enhances the channel activity. Our results demonstrated that the C-terminal interaction provides a basis for fast regulation of the R-type anion channel.

307   **Gating of the QUAC1 channel**

308   Our electrophysiological experiments have demonstrated that malate plays a vital role in

309   modulating *Gm*QUAC1 activity; however, we wonder how malate regulation is coupled to

310   channel activation. The *Gm*QUAC1 structure reveals that the conserved pore-lining tryptophan

311   W90 is in close contact with an unmodelled density within the fenestration (Fig. 4b). To

312   understand the functional role of W90, we made mutations of W90A and W90F. Compared to

313   wild-type, the removal of indole ring in W90A mutant causes ~5 times larger conductance in

314   the presence of external malate. A similar aromatic amino acid substitution in the W90F mutant

315   can stimulate channel currents even larger (Extended Data Fig. 9a and 9b). These observations

316   imply that the conserved W90 may interact with surrounding residues and function as a toggle

317   switch to regulate channel gating.

318   This notion is confirmed in the measurement of combined mutants of W90F with other

319   two loss-of-function mutants, Δ1-53 and A477E. We observed that both null mutants restore

320   channel activity to a moderate level after the addition of W90F (Extended Data Fig. 9c and 9d).

321   We speculate that malate promotes QUAC1 activation probably via regulating the

322   conformation of tryptophan W90. Distinct from the S-type SLAC1 regulation controlled by

323   phosphorylation/ dephosphorylation [16–20], our study reveals that the R-type QUAC1 gating can

324   be directly mediated by malate, which is much faster. These findings may explain the fast

325   kinetics observed in the R-type channel, compared with the slow activity found in the S-type

326   channel.

327

328   **DISCUSSION**

329   Recently, AlphaFold has made significant progress in 3D structure prediction from protein

330   sequence [51]. By taking advantage of this advanced technology, we generated an AlphaFold

331   predicted model for the *Gm*QUAC1 protein that is the focus of our current study. Surprisingly,

332   the AlphaFold predicted *Gm*QUAC1 structure (AF-structure) is surprisingly similar to that

333   determined by cryo-EM (cryo-EM structure), with an r.m.s.d. of 2.1 Å/160 C_α and 1.4 Å/207

334   C_α for the TMD and CHD, respectively. However, further superimposition reveals a noticeable

12

335   difference in the orientation of TMD vs CHD in QUAC1, with an r.m.s.d. of 3.1 Å/388 C_α and

336   3.2 Å/776 C_α for the monomer and dimer, respectively (Extended Data Fig. 10a).

337   Unlike the kinked TM6 observed in the cryo-EM structure, the TM6 in the AF-structure

338   adopts a straight conformation, eliminating the lateral fenestration in TMD (Extended Data Fig.

339   10b). As the malate regulation effect on the channel is not taken into account, the resulting

340   predicted model may represent an apo-structure in a low energy state. The cryo-EM structure

341   determined in the presence of malate reveals a high-energy twisted conformation, thus

342   representing a malate-activated structure. These two structures allow us to make comparisons

343   and gain insight into the gating mechanism of the QUAC1 channel. It seems that the pore-

344   forming helices move slightly outward, as suggested by the porcupine plot on the $C\alpha$

345   comparison between the AF-structure and the cryo-EM structure (Extended Data Fig. 10c).

346   Another noticeable difference is the dihedral angle between the TMD and CHD interfaces,

347   which is 86.5º and 83.0º for the AF-structure and cryo-EM structure, respectively (Extended

348   Data Fig. 10d). This observation shows a slight rotation (~3.5º) between these two states,

349   suggesting that domain reorganization occurs during the conformational conversion. We

350   speculate that the domain reorganization is associated with malate regulation, and subsequently

351   triggers conformational changes of the toggle switch in the pore to activate the channel

352   (Extended Data Fig. 10e and and Supplementary Video 1).

353   Our work provides the first glimpse of the molecular structures of the R-type anion channel.

354   Our study showed that the TMD and CHD portions in QUAC1 interact in a twisted manner,

355   rendering the channel in a high-energy state. Based on our data, we propose the following

356   mechanism for QUAC1 activation: upon malate binding, the QUAC1 undergoes intramolecular

357   domain reorganization to form a twisted bi-layer architecture, which subsequently induces the

358   conformational change of the toggle switch W90. These changes promote the channel

359   conversion from the basal to the activated state. The malate-mediated activation is further

360   enhanced by other modulations, such as kinase phosphorylation or calmodulin-binding,

361   probably via releasing its inhibitory domain-swapped helix from the inter-protomer interaction

362   (Fig. 7g and Supplementary Video 2). Our study provides mechanistic insights into the gating

13

363   activation of the R-type channel and offers a plausible explanation for fast kinetics in the R-

364   type currents.

365   As both SLAC1 and QUAC1 represent two essential distinct channels that mediate

366   osmotic active anions efflux from guard cell, one remaining puzzle is how they interplay with

367   each other to initiate stomatal closure in response to various environmental stimuli. Further

368   investigation to address this issue will shed light on the understanding of guard cell stomatal

369   signaling and provide critical information for engineering drought-resistant or water-use

370   efficiency crops.

371

SUPPLEMENTAL INFORMATION

Supplemental information can be found online at XXX

DECLARATION OF INTERESTS

The authors declare no competing financial interests.

AUTHOR CONTRIBUTIONS

L.Q. performed protein purification, Cryo-EM data collection, TEVC experiments, and data analysis; L.-h.T., J.-s.X., Y.Z. performed Cryo-EM data collection and structural determination; X.-h.Z. performed mutagenesis and protein purification; M.S. performed PLB experiments and data analysis; C.-r.Z., X.-l.L., M.-h.W, performed experiments; F.L., F.S., Y.-j.Z. analyzed data; Y.-h.C. initiated the project, planned and analyzed experiments, supervised the research and wrote the manuscript with input from all authors.

REFERENCES

1.   Hetherington, A & Woodward, F. The role of stomata in sensing and driving environmental change. *Nature* **424**, 901–908 (2003).

2.   Sirichandra, C., Wasilewska, A., Vlad, F., Valon, C. & Leung, J. The guard cell as a single-cell model towards understanding drought tolerance and abscisic acid action. *J. Exp. Bot.* **60**, 1439–1463 (2009).

3.   Kim, T.-H., Böhmer, M., Hu, H., Nishimura, N. & Schroeder, J. I. Guard cell signal transduction network: advances in understanding abscisic acid, CO_2 , and Ca^{2+} signaling. *Annu. Rev. Plant Biol.* **61**, 561–591 (2010).

401   4.   Murata, Y., Mori, I. C. & Munemasa, S. Diverse stomatal signaling and the signal integration mechanism.
402   *Annu. Rev. Plant Biol.* **66**, 369–392 (2015).

403   5.   Kollist, H., Nuhkat, M. & Roelfsema, M. R. G. Closing gaps: linking elements that control stomatal
404   movement. *New Phytol.* **203**, 44–62 (2014).

405   6.   Roelfsema, M. R. G., Hedrich, R. & Geiger, D. Anion channels: master switches of stress responses.
406   *Trends Plant Sci.* **17**, 221–229 (2012).

407   7.   Pantoja, O. Recent advances in the physiology of ion channels in plants. *Annu. Rev. Plant Biol.* **72**, 463-
408   495 (2021).

409   8.   Hedrich, R. Ion channels in plants. *Physiol. Rev.* **92**, 1777–1811 (2012).

410   9.   Keller, B. U., Hedrich, R. & Raschke, K. Voltage-dependent anion channels in the plasma membrane of
411   guard cells. *Nature* **341**, 450–453 (1989).

412   10.   Schroeder, J. I. & Keller, B. U. Two types of anion channel currents in guard cells with distinct voltage
413   regulation. *Proc. Natl. Acad. Sci. USA* **89**, 5025–5029 (1992).

414   11.   Schroeder, J. I. *et al.* Cytosolic calcium regulates ion channels in the plasma membrane of *Vicia faba*
415   guard cells. *Nature* **338**, 427–430 (1989).

416   12.   Hedrich, R., Busch, H. & Raschke, K. Ca^{2+} and nucleotide dependent regulation of voltage dependent
417   anion channels in the plasma membrane of guard cells. *EMBO J.* **9**, 3889–3892 (1990).

418   13.   Vahisalu, T. *et al.* SLAC1 is required for plant guard cell S-type anion channel function in stomatal
419   signalling. *Nature* **452**, 487–491 (2008).

420   14.   Negi, J. *et al.* CO_2 regulator SLAC1 and its homologues are essential for anion homeostasis in plant cells.
421   *Nature* **452**, 483–486 (2008).

422   15.   Saji, S. *et al.* Disruption of a gene encoding C4-dicarboxylate transporter-like protein increases ozone
423   sensitivity through deregulation of the stomatal response in *Arabidopsis thaliana*. *Plant Cell Physiol.* **49**,
424   2–10 (2008).

425   16.   Geiger, D. *et al.* Activity of guard cell anion channel SLAC1 is controlled by drought-stress signaling
426   kinase-phosphatase pair. *Proc. Natl. Acad. Sci. USA* **106**, 21425–21430 (2009).

427   17.   Lee, S. C., Lan, W., Buchanan, B. B. & Luan, S. A protein kinase-phosphatase pair interacts with an ion
428   channel to regulate ABA signaling in plant guard cells. *Proc. Natl. Acad. Sci. USA* **106**, 21419–21424

16

429   (2009).

430   18.   Brandt, B. *et al.* Reconstitution of abscisic acid activation of SLAC1 anion channel by CPK6 and OST1

431   kinases and branched ABI1 PP2C phosphatase action. *Proc. Natl. Acad. Sci. USA* **109**, 10593–10598

432   (2012).

433   19.   Maierhofer, T. *et al.* Site-and kinase-specific phosphorylation-mediated activation of SLAC1, a guard cell

434   anion channel stimulated by abscisic acid. *Sci. Signal.* **7**, 1–12 (2014).

435   20.   Deng, Y. N. *et al.* Structure and activity of SLAC1 channels for stomatal signaling in leaves. *Proc. Natl.*

436   *Acad. Sci. USA* **118**, 1–8 (2021).

437   21.   Chen, Y.-H. *et al.* Homologue structure of the SLAC1 anion channel for closing stomata in leaves. *Nature*

438   **467**, 1074–1080 (2010).

439   22.   Meyer, S. *et al. At*ALMT12 represents an R-type anion channel required for stomatal movement in

440   Arabidopsis guard cells. *Plant J.* **63**, 1054–1062 (2010).

441   23.   Sasaki, T. *et al.* Closing plant stomata requires a homolog of an aluminum-activated malate transporter.

442   *Plant Cell Physiol.* **51**, 354–365 (2010).

443   24.   Jalakas, P. *et al.* Combined action of guard cell plasma membrane rapid- and slow-type anion channels in

444   stomatal regulation. *Plant Physiol.* (2021) doi:10.1093/plphys/kiab202.

445   25.   Gutermuth, T. *et al.* Tip-localized Ca^{2+}-permeable channels control pollen tube growth via kinase-

446   dependent R- and S-type anion channel regulation. *New Phytol.* **218**, 1089-1105 (2018).

447   26.   Herbell, S., Gutermuth, T. & Konrad, K. R. An interconnection between tip-focused Ca^{2+} and anion

448   homeostasis controls pollen tube growth. *Plant Signal. Behav.* **13,** 1559-2324 (2018).

449   27.   Mumm, P. *et al.* C-terminus-mediated voltage gating of arabidopsis guard cell anion channel QUAC1.

450   *Mol. Plant* **6,** 1550-1563 (2013).

451   28.   Hedrich, R. *et al.* Malate-sensitive anion channels enable guard cells to sense changes in the ambient CO_2

452   concentration. *Plant J.* **6,** 741-748 (1994).

453   29.   Raschke, K. Alternation of the slow with the quick anion conductance in whole guard cells effected by

454   external malate. *Planta* **217,** 651-657 (2003).

455   30.   Imes, D. *et al.* Open stomata 1 (OST1) kinase controls R-type anion channel QUAC1 in *Arabidopsis*

456   guard cells. *Plant J.* **74**, 372–382 (2013).

457   31.   Luu, K., Rajagopalan, N., Ching, J. C. H., Loewen, M. C. & Loewen, M. E. the malate-activated

458   ALMT12 anion channel in the grass Brachypodium distachyon is co-activated by Ca^{2+}/calmodulin. *J.*

459   *Biol. Chem.* **294,** 6142-6156 (2019).

460   32.   Meyer, S. *et al.* Malate transport by the vacuolar *At*ALMT6 channel in guard cells is subject to multiple

461   regulation. *Plant J.* **67,** 247–257 (2011).

462   33.   De Angeli, A., Zhang, J., Meyer, S. & Martinoia, E. *At*ALMT9 is a malate-activated vacuolar chloride

463   channel required for stomatal opening in *Arabidopsis*. *Nat. Commun.* **4,** 1–10 (2013).

464   34.   Kovermann, P. *et al.* The *Arabidopsis* vacuolar malate channel is a member of the ALMT family. *Plant J.*

465   **52,** 1169–1180 (2007).

466   35.   Sasaki, T. *et al.* A wheat gene encoding an aluminum-activated malate transporter. *Plant J.* **37,** 645–653

467   (2004).

468   36.   Hoekenga, O. A. *et al. At*ALMT1, which encodes a malate transporter, is identified as one of several

469   genes critical for aluminum tolerance in Arabidopsis. *Proc. Natl. Acad. Sci. USA* **103,** 9738–9743 (2006).

470   37.   Collins, N. C., Shirley, N. J., Saeed, M., Pallotta, M. & Gustafson, J. P. An ALMT1 gene cluster

471   controlling aluminum tolerance at the Alt4 Locus of Rye (*Secale cereale L.*). *Genetics***179,** 669–682

472   (2008).

473   38.   Ligaba, A., Katsuhara, M., Ryan, P. R., Shibasaka, M. & Matsumoto, H. The *Bn*ALMT1 and *Bn*ALMT2

474   genes from rape encode aluminum-activated malate transporters that enhance the aluminum resistance of

475   plant cells. *Plant Physiol.* **142,** 1294-1303 (2006).

476   39.   Piñeros, M. A. *et al.* Not all ALMT1-type transporters mediate aluminum-activated organic acid

477   responses: The case of *Zm*ALMT1 - An anion-selective transporter. *Plant J.* **53,** 352–367 (2008).

478   40.   Ligaba, A., Maron, L., Shaff, J., Kochian, L. & Piñeros, M. Maize *Zm*ALMT2 is a root anion transporter

479   that mediates constitutive root malate efflux. *Plant, Cell Environ.* **35,** 1185-1200 (2012).

480   41.   Bai, Y. *et al.* A natural mutation-led truncation in one of the two aluminum-activated malate transporter-

481   like genes at the Ma locus is associated with low fruit acidity in apple. *Mol. Genet. Genomics* **287,** 663–

482   678. (2012).

483   42.   De Angeli, A. *et al.* The vacuolar channel *Vv*ALMT9 mediates malate and tartrate accumulation in berries

484   of *Vitis vinifera*. *Planta* **238,** 283-291 (2013).

485   43.   Rudrappa, T., Czymmek, K. J., Paré, P. W. & Bais, H. P. Root-secreted malic acid recruits beneficial soil

486   bacteria. *Plant Physiol.* **148,** 1547-1556 (2008).

487   44.   Takanashi, K. *et al.* A dicarboxylate transporter, *Lj*ALMT4, mainly expressed in nodules of lotus

488   japonicus. *Mol. Plant-Microbe Interact.* **29**, 584–592 (2016).

489   45.   Xu, M. *et al.* The barley anion channel, *Hv*ALMT1, has multiple roles in guard cell physiology and grain

490   metabolism. *Physiol. Plant.* **153,** 183-193 (2015).

491   46.   Heng, Y. *et al. Os*ALMT7 maintains panicle size and grain yield in rice by mediating malate transport.

492   *Plant Cell* **30**, 889–906 (2018).

493   47.   Holm, L. DALI and the persistence of protein shape. *Protein Sci.* **29**, 128–140 (2020).

494   48.   Furuichi, T. *et al.* An extracellular hydrophilic carboxy-terminal domain regulates the activity of

495   *Ta*ALMT1, the aluminium-activated malate transport protein of wheat. *Plant J.* **64,** 47-55 (2010).

496   49.   Smart, O. S., Neduvelil, J. G., Wang, X., Wallace, B. A. & Sansom, M. S. P. HOLE: A program for the

497   analysis of the pore dimensions of ion channel structural models. *J. Mol. Graph.* **14**, 354–360 (1996).

498   50.   Peng, W. *et al.* Characterization of the soybean *Gm*ALMT family genes and the function of *Gm*ALMT5

499   in response to phosphate starvation. *J. Integr. Plant Biol.* **60**, 216–231 (2018).

500   51.   Jumper, J. *et al.* Highly accurate protein structure prediction with AlphaFold. *Nature* (2021)

501   doi:10.1038/s41586-021-03819-2.

502   52.   Altschul, S. Gapped BLAST and PSI-BLAST: a new generation of protein database search programs.

503   *Nucleic Acids Res.* **25**, 3389–3402 (1997).

504   53.   Wang, X.-H. *et al.* Structural basis for the activity of TRIC counter-ion channels in calcium release. *Proc.*

505   *Natl. Acad. Sci. USA* **116**, 4238–4243 (2019).

506   54.   Mastronarde, D. N. Automated electron microscope tomography using robust prediction of specimen

507   movements. *J. Struct. Biol.* **152,** 36-51. (2005).

508   55.   Wu, C., Huang, X., Cheng, J., Zhu, D. & Zhang, X. High-quality, high-throughput cryo-electron

509   microscopy data collection via beam tilt and astigmatism-free beam-image shift. *J. Struct. Biol.* **208**,

510   107396 (2019).

511   56.   Zivanov, J. *et al.* New tools for automated high-resolution cryo-EM structure determination in RELION-

512   3. *Elife* **7**, 1–22 (2018).

19

513   57.   Punjani, A., Rubinstein, J. L., Fleet, D. J. & Brubaker, M. A. cryoSPARC: algorithms for rapid

514   unsupervised cryo-EM structure determination. *Nat. Methods* **14**, 290–296 (2017).

515   58.   Asarnow, D., Palovcak, E. & Cheng, Y. UCSF pyem. (2021).

516   59.   Pettersen, E. F. *et al.* UCSF Chimera--a visualization system for exploratory research and analysis. *J.*

517   *Comput. Chem.* **25**, 1605–1612 (2004).

518   60.   Zheng, S. Q. *et al.* MotionCor2: anisotropic correction of beam-induced motion for improved cryo-

519   electron microscopy. *Nat. Methods* **14**, 331–332 (2017).

520   61.   Zhang, K. Gctf: Real-time CTF determination and correction. *J. Struct. Biol.* **193**, 1–12 (2016).

521   62.   Zhang, K., and Sun, F. Gautomatch: an efficient and convenient gpu-based automatic particle selection

522   program. *https://www2.mrc-lmb.cam.ac.uk/download/gautomatch-056.* (2011).

523   63.   Liebschner, D. *et al.* Macromolecular structure determination using X-rays, neutrons and electrons: recent

524   developments in ıt Phenix. *Acta Crystallogr. Sect. D* **75**, 861–877 (2019).

525   64.   Kucukelbir, A., Sigworth, F. J. & Tagare, H. D. Quantifying the local resolution of cryo-EM density

526   maps. *Nat. Methods* **11,** 63-65 (2014).

527   65.   Emsley, P., Lohkamp, B., Scott, W. G. & Cowtan, K. Features and development of Coot. *Acta*

528   *Crystallogr. Sect. D .* **66**, 486–501 (2010).

529   66.   Gabler, F. *et al.* Protein sequence analysis using the MPI bioinformatics toolkit. *Curr. Protoc.*

530   *Bioinforma.* **72**, e108 (2020).

531   67.   Barad, B. A. *et al.* EMRinger: Side chain-directed model and map validation for 3D cryo-electron

532   microscopy. *Nat. Methods* **12**, 943–946 (2015).

533   68.   Pettersen, E. F. *et al.* UCSF ChimeraX: Structure visualization for researchers, educators, and developers.

534   *Protein Sci. A Publ. Protein Soc.* **30**, 70–82 (2021).

535   69.   Bi, G. *et al.* The ZAR1 resistosome is a calcium-permeable channel triggering plant immune signaling.

536   *Cell* **184**, 3358-3360 (2021).

537

538 **METHODS**

539 **Bioinformatics analysis of ALMT proteins**

540 Sequences related to QUAC1/ALMTs were searched and analyzed by using PSI-BLAST [52].

541 Searches at E<5*10^{-3} starting with thirteen individual *Arabidopsis* ALMTs identified a

542 common pool of over 1,700 plant ALMT-related protein sequences, which were pooled

543 together and used for sub-classification into families and subfamilies. Detailed information is

544 reported in the footnotes to the Extended Data Table 1.

545

546 **Cloning and expression of QUAC1/ALMT12 in yeast *S. pombe***

547 Full-length coding sequences of six plant QUAC1s from rice, wheat, corn, soybean, tomato and

548 cotton, were cloned into a modified pREP1 vector with a C-terminal 10× His tag. The resulting

549 constructs were transformed into a leucine auxotrophic *S. pombe* strain, and the transformants

550 were selected on the standard EMM plates without leucine, as previously described [53]. To

551 prevent protein expression during strain growth, 25 μM thiamine was added to inhibit the

552 promoter.

553

554 **Scaled-up production and purification of *Gm*QUAC1**

555 To prepare the seed, transformed cells were inoculated into 100 ml EMM culture medium

556 supplemented with 25 μM thiamine and were shaken at 200 rpm and 30°C for 24 hr. For protein

557 expression and scaled-up production, the seed cells were collected by centrifugation and

558 washed with sterile water twice before inoculation to a culture of 500 ml. After 12 hr growth,

559 500 ml of fresh medium was supplemented, and the culture continued to grow for an additional

560 24 hr. Cells were harvested through centrifugation for 20 min at 4,500 rpm.

561 For protein purification, cells were re-suspended in lysis buffer (50 mM Tris-HCl pH 8.0,

562 200 mM NaCl, 2.5% glycerol, 1 μg/ml aprotinin, 1 μg/ml leupeptin, 1 μg/ml pepstatin, 2 mM

563 PMSF and 2 mM DTT) and lysed using a high-pressure cell disrupter (JNBIO) with 4 passes

564 at ~18,000 psi. Cell debris was removed by centrifugation at 12,000 rpm for 15 min, and the

565 supernatant was subjected to a further ultra-centrifugation at 41,000 rpm for 1 hr. The

566   membrane was collected and homogenized in a solubilization buffer (50 mM Tris-HCl pH 8.0,

567   200 mM NaCl and 2.5% glycerol) and incubated with a final concentration of 1.0% DDM and

568   0.02% CHS by gentle stirring for 1 hr at 4°C. After ultra-centrifugation at 35,000 rpm for 50

569   min, the resulting supernatant was purified by Ni^{2+}-affinity column pre-equilibrated with the

570   same solubilization buffer supplemented with 0.05% DDM and 2 mM TCEP. After 20 columns

571   volume of buffer wash, the protein was eluted with 350 mM imidazole in the solubilization

572   buffer. The resulting *Gm*QUAC1 protein, without removal of His-tag, was concentrated to ~10

573   mg/ml and loaded onto a Superose6 (10/300) gel-filtration column for further purification and

574   detergent exchange. The gel-filtration buffer contained 20 mM Tris, 150 mM NaCl (pH 8.0,

575   adjusted with HCl) or 75 mM L-malate (pH 8.0, adjusted with NaOH), and 0.005% LMNG.

576   The elution fractions were analyzed by SDS-PAGE, and the peak fractions were collected and

577   concentrated for functional analysis (~2 mg/ml) or making cryo-EM grids (~5 mg/ml).

578

579   Cryo-EM grid preparation and data acquisition

580   4 μl of *Gm*QUAC1^{malate} proteins (purified in 75 mM L-malate) were applied to newly glow-

581   discharged holy carbon film grids (Au R1.2/1.3, 300 meshes, Quantifoil, Germany). The grids

582   were blotted with force 3 and blotting time of 9.0 s at 100% humidity and 4°C and were vitrified

583   by plunge freezing into liquid ethane using Vitrobot Mark IV (Thermo Fisher Scientific, USA).

584   All movies were collected on a Titan Krios G2 transmission electron microscope (Thermo

585   Fisher Scientific, USA) operated at 300 KV, equipped with a Gatan K2 Summit direct detection

586   camera (Gatan Company, USA) and a post-column GIF energy filter.

587   Data collection was performed on EF-TEM mode with a silt width of 20 $e^-\cdot V$. The

588   magnification was set to a nominal 130,000x, corresponding to a calibrated pixel size of 1.04

589   Å/pixel at the specimen level (0.52 Å/pixel in super-resolution mode). Images were recorded

590   using SerialEM (version 3.8.4) [54] with a beam-image shift method [55]. During the 8s exposure,

591   32 frames were collected with a dose of around 60 $e^-/Å^2$. A total of 6,189 movie stacks were

592   collected, with defocus ranging from −1.2 μm to −2.2 μm.

593

Image processing and model building

594

595 For cryo-EM image processing, all main steps were performed using RELION 3.0 [56] or

596 cryoSPARC 3.1 [57]. Pyem [58] and UCSF Chimera [59] were used for format conversion of data files

597 and reconstructions analysis, respectively.

598 In brief, 6,189 movie stacks were aligned by 5×5 patches with dose weighting and binned

599 to 1.04 Å using Motioncor2 [60]. The contrast transfer function parameters were estimated using

600 GCTF [61]. Micrographs with defects in the thon rings were discarded. 2,987,283 candidate

601 particles were initially picked using Gautomatch without template [62], and followed by several

602 rounds of 2D classification in cryoSPARC, giving a set of 2,136,754 high-quality particles. A

603 rough initial model was generated by a subset of 100,000 particles. Subsequentially, six rounds

604 of 3D classification were performed at C1 symmetry. Three parallel 3D classifications were

605 performed within each round, and the resulting good particles were combined for sequential

606 round classification. After that, a set of 428,433 particles that generated a map of 4.0 Å using

607 NU-Refinement in cryoSPARC were subjected to Bayesian polishing. Three rounds of 3D

608 classification were further performed as described below. Each round contains an NU-

609 Refinement at C2 symmetry in cryoSPARC followed by an alignment-free 3D classification

610 with a micelle-free mask in Relion. Finally, NU-refinement of 169,576 particles yielded a

611 reconstruction with a resolution of 3.5 Å, based on the gold-standard Fourier Shell Correlation

612 (FSC) using the 0.143 criterion. Density modification was performed using PHENIX [63]. Local

613 resolution was determined using ResMap [64].

614 A *de novo* atomic model was built manually in Coot [65] using the predicted secondary

615 structure from MPI quick2d [66]. The model was further refined using PHENIX [63]. The final

616 model was validated using EMRinger [67]. All structure figures were prepared in UCSF

617 ChimeraX [68].

618

The two-electrode voltage-clamp recordings

620 The TEVC recordings were conducted as previously described [20]. In brief, all cDNAs for

621 *Gm*QUAC1, including wild-type or mutants, were cloned into plasmid pGHME2 for expression

622   in *Xenopus laevis* oocyte. Linearised plasmids were used to generate cRNAs using T7

623   polymerase. 36 nanograms of cRNA of each construct were injected into isolated oocytes.

624   Oocytes were then incubated at 18°C for ~48 hr in ND96 buffer (96 mM NaCl, 1.8 mM $CaCl_2$,

625   1 mM $MgCl_2$, 2 mM KCl, 5 mM HEPES-Na, pH 7.5).

626   Using a Oocyte Clamp OC-725C amplifier (Warner Instruments) and a Digidata 1550 B

627   low-noise data acquisition system with pClamp software (Molecular Devices), TEVC

628   recordings were performed in the bath solutions: 10 mM MES/Tris pH 5.6, 1mM

629   Ca(gluconate)$_2$, 1 mM Mg(gluconate)$_2$, 70 mM Na(gluconate), 1 mM $LaCl_3$, 30 mM NaCl or

630    $NaNO_3$, or 30 mM L-malate (pH 5.6, prepared from L-malic acid with NaOH). Osmolarity was

631   adjusted to ~220 mOsmol*kg^{-1} with D-Sorbitol. The microelectrode solutions contained 3 M

632   KCl, and the bath electrode was a 3 M KCl agar bridge. Voltage-clamp currents were measured

633   in response to 200 ms-long voltage steps to test potentials that ranged from +60 mV to –180

634   mV in 20 mV decrement. Prior to each voltage step, the membrane was held at +60 mV for 50

635   ms, and following each voltage step, the membrane was returned to –180 mV for 50 ms. I-V

636   relations for *Gm*QUAC1 channels were generated from currents measured at 5 ms after the

637   beginning (Instantaneous currents, I_{inst}) or before the end (Steady-state currents, I_{ss}) of each test

638   voltage step. Three independent batches of oocytes were investigated and showed consistent

639   findings. Data from one representative oocyte batch were shown. The recordings were analyzed

640   using Clampfit 10.6 (Molecular Devices) and Prism (ver. 5.0, GraphPad).

641

642   **The planar lipid bilayer recordings**

643   Lipid bilayer experiments were conducted as previously described in our study of the ZAR1

644   channel [69]. The purified *Gm*QUAC1 (in 150 mM NaCl or 75 mM L-malate), at a concentration

645   of 1.5~2.5 μg/ml, was fused into planar lipid bilayers formed by painting a lipid mixture of

646   phosphatidylethanolamine (DOPE) and phosphatidylcholine (DOPC) (Avanti Polar Lipids) in

647   a 5:3 ratio in decane across a 200 μm hole in a polystyrene partition separating the internal and

648   external solutions in polysulfonate cups (Warner Instruments). The *trans* chamber (1.0 ml),

649   representing the extracellular compartment, was connected to the head stage input of a bilayer

24

650   voltage-clamp amplifier. The *cis* chamber (1.0 ml), representing the cytoplasmic compartment,

651   was held at virtual ground. Solutions used for I-V relationship analysis were as follows: 150

652   mM NaCl or 150 mM NaNO$_3$. All solutions were buffered with 20 mM Tris (pH 8.0). Purified

653   proteins were added to the *cis* side and fused with the lipid bilayer.

654   Currents were recorded every 1~2 min after application of the voltage to the *trans* side.

655   Single-channel currents were recorded using a Bilayer Clamp BC-525D (Warner Instruments),

656   filtered at 800 Hz using a Low-Pass Bessel Filter 8 Pole (Warner Instruments) and digitized at

657   4 kHz. All experiments were performed at room temperature ($23 \pm 2°C$). The recordings were

658   analyzed using Clampfit 10.6 (Molecular Devices) and Prism (ver. 5.0, GraphPad).

659

660   **Biochemical characterization of CHD of *Gm*QUAC1**

661   cDNAs encoding the C-terminal cytoplasmic helical domain of *Gm*QUAC1 (wild-type or

662   mutants) were subcloned into a modified bacterial expression vector pET-24a, with a C-

663   terminal 10× His tag. Transformed *E. coli* BL21 (DE3) cells were grown in a TB medium

664   containing Kanamycin (50 μg/ml). Protein expression was induced in cells grown to an optical

665   density at OD600 of ~0.8 with 0.4 mM isopropyl β-D-thiogalactoside (IPTG) and followed by

666   overnight cell growth at 16°C. Cells were collected and subsequently lysed using a high-

667   pressure cell disrupter (JNBIO) with 3 passes at ~15,000 psi. The target protein was purified

668   by using Ni^{2+} affinity chromatography and further analyzed by Superdex75 (10/300) gel

669   filtration chromatography and SDS-PAGE.

670

671   **The three-dimensional structure modelling using AlphaFold2**

672   Briefly, the sequence for AlphaFold prediction was generated by two individual

673   *Gm*QUAC1 sequences, connecting by a linker of tandemly repeated sequence of (GSGS)$_{50}$.

674   Running with the local installed AlphaFold2 program and the CASP14 preset and databases (as

675   of July 23, 2021), five dimer models were generated, with their pLDDT (predicted lDDT-Cα)

676   scores ranging from 64.6 to 68.8. All the AlphaFold predicted structures (AF-structure) are

677   nearly identical, with apparent two-fold symmetry. The two protomers in the top-rank dimer

25

678 model (scored 68.8) display an r.m.s.d of 0.92 Å, was selected for further structural comparison

679 with the cryo-EM structure. For a better view, the disordered (residues 1-35, 394-454 and 507-

680 537) regions were removed in the final model.

681

682 **QUANTIFICATION AND STATISTICAL ANALYSIS**

683 In all figure legends, n represents the number of independent biological replicates. All

684 quantitative data were presented as mean ± SEM.

685

686 **DATA AND CODE AVAILABILITY**

687 All data are available in the manuscript or the supplementary material. The accession number

688 for the 3D cryo-EM density map reported in this paper is XXX, and the Protein Data Bank
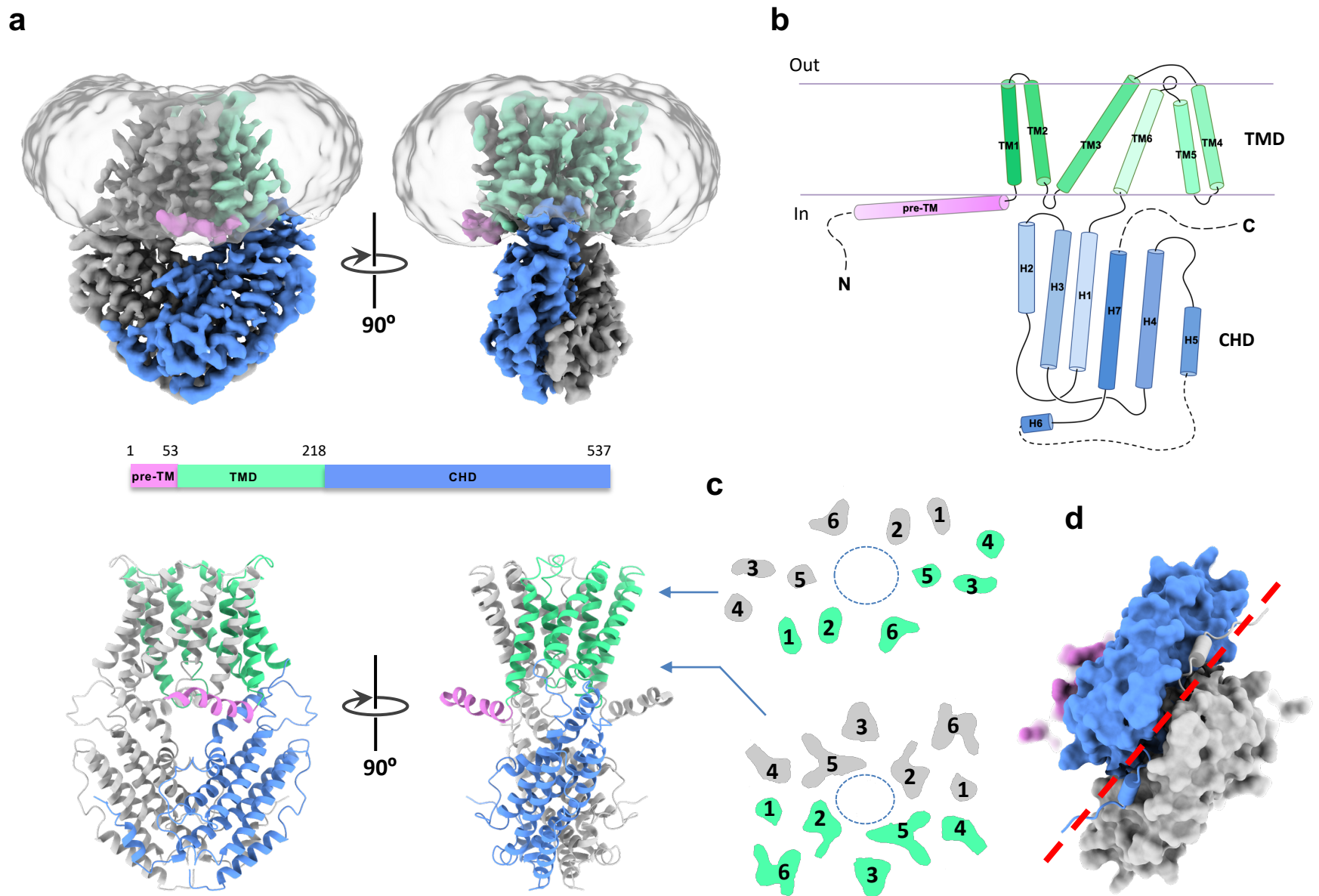
689 (PDB) accession code for the coordinate is XXX.

690

691 **ADDITIONAL RESOURCES**

692 This study did not generate any additional resources.

693

Figure 1

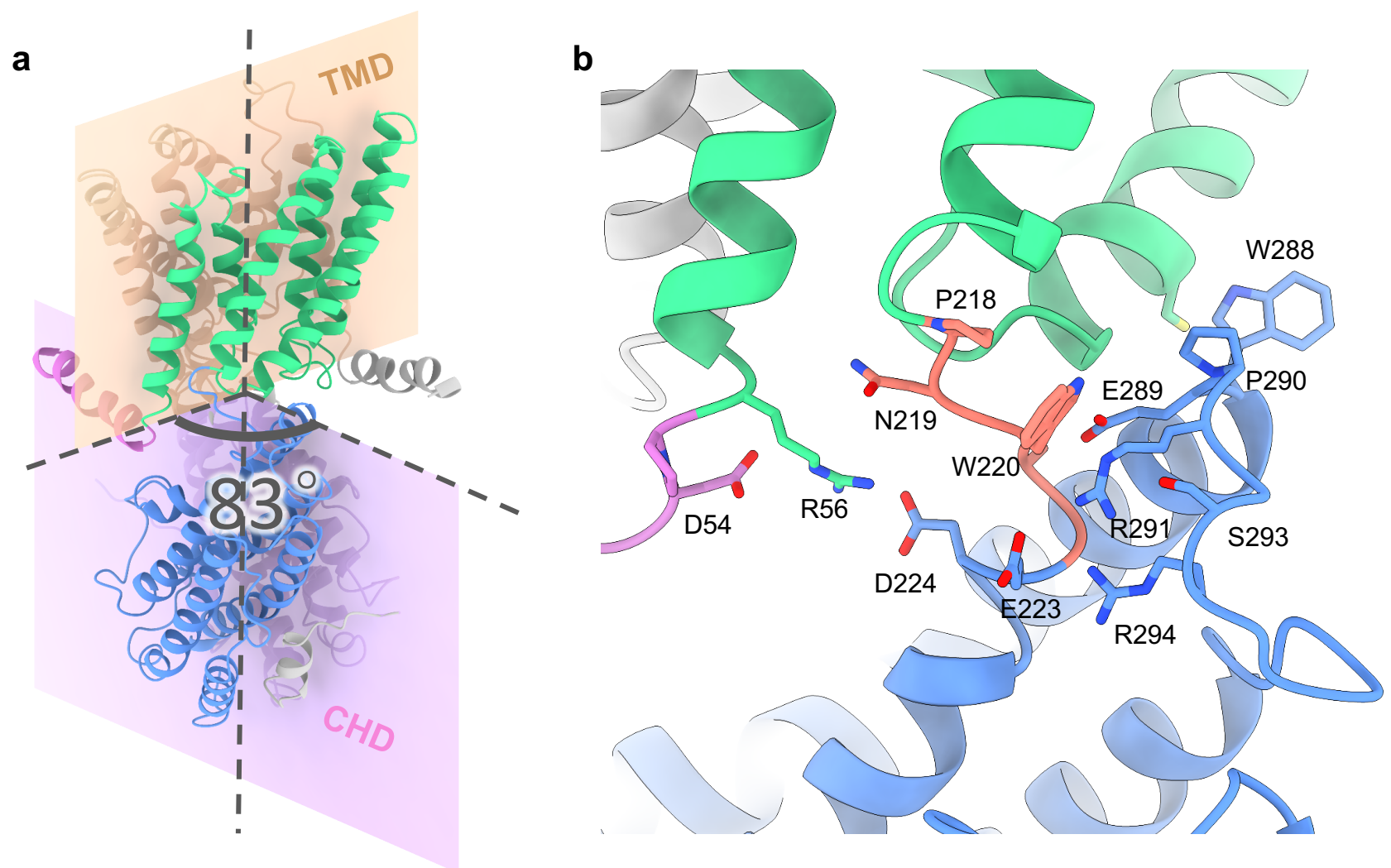**Fig. 1 Architechture of the QUAC1 channel**

a, Overall structure of the *Gm*QUAC1 channel. The cryo-EM density maps (top) and ribbons drawings (bottom) are shown, with the pre-TM helix in pink, the transmembrane domain (TMD) in green and the cytoplasmic helical domain (CHD) in blue in one promoter. Another promoter is coloured in grey.

b, Topology of the *Gm*QUAC1 protomer. The six helices in TMD are marked by TM1-6, and the seven helices in CHD are marked as H1-7. The membrane boundary is shown as grey lines. The disordered regions are indicated as dashed lines.

c, Top view of the cross-section of the transmembrane layer at the indicated positions by the arrow lines in (**a**). The elliptical dashed line marks the pore, and the TMs are indicated.

d, Bottom view of the C-terminal dimeric domains, colored as in (**a**). The domain-swapped finger helix H6 is shown as cylinder cartoon, and a red dash line marks the dimeric interface of the CHD.

Figure 2

Fig. 2 The twisted bi-layer architecture of the QUAC1 channel

a, The dimeric interfaces of the TMD and CHD of the *Gm*QUAC1 channel. These dimeric interfaces are nearly perpendicular to each other, forming a dihedral angle of ~83º. The ribbon model is colored as in Fig. **1a**.

b, The layer interface between the TMD and CHD. The TMD portion connects to the CHD portion via a highly conserved PXWXG motif (P218-N219-W220-S221-G222, in salmon), which is interact with another characteristic motif WEP (W288-E289-P290, located between helix H2 and H3, in blue). Other surrounding charged residues at the interface are also shown in sticks, including R56, R291, R294, D54, E223, D224 and E289. The ribbon model is colored as in (**a**).

Figure 3
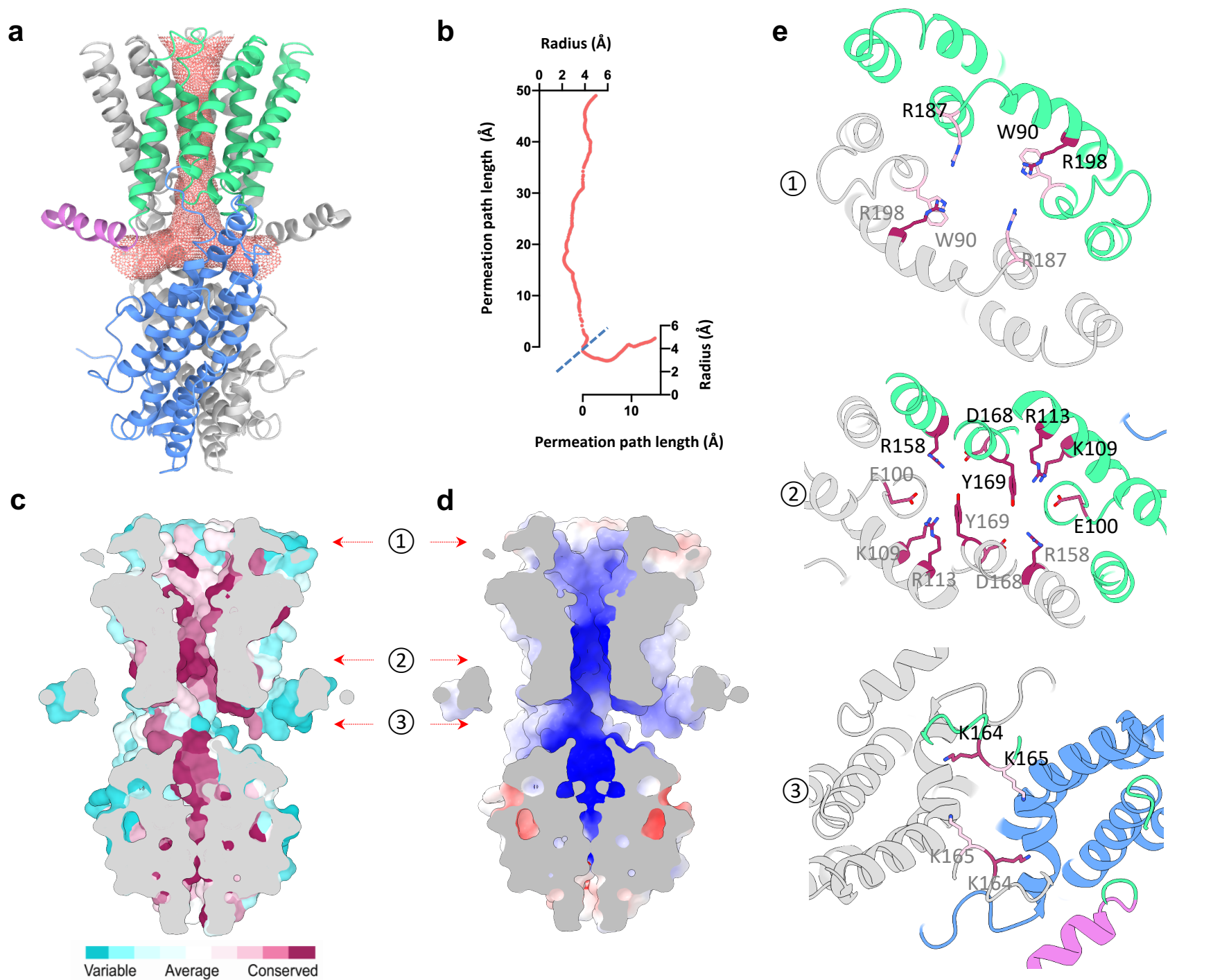
**Fig. 3 Structural feature of the QUAC1 channel pore**

a, The pore-lining surface was computed by the program HOLE and drawn into a ribbon model of the *Gm*QUAC1 pore. We used a simple van der Waals surface for the protein and the program default probe radius of 1.15 Å. The T-shaped pore is shown in salmon dots.

b, Plot of the pore radius as a function of the pore axis.

c and **d,** Side views of the cross-section through the ion-conducting pore. The molecular surface colored with sequence conservation for 137 non-redundant proteins of the QF2B subfamily is shown in (**c**) and the molecular surface colored with electrostatic potential is shown in (**d**).

e, Top views of the cross-section through the ion-conducting pore at three indicated positions by the arrow in (**c**) and (**d**). The ribbon is colored as in (**a**). The conserved pore-lining charged residues are shown in sticks, coloured with the sequence conservation as in (**c**).

Figure 4
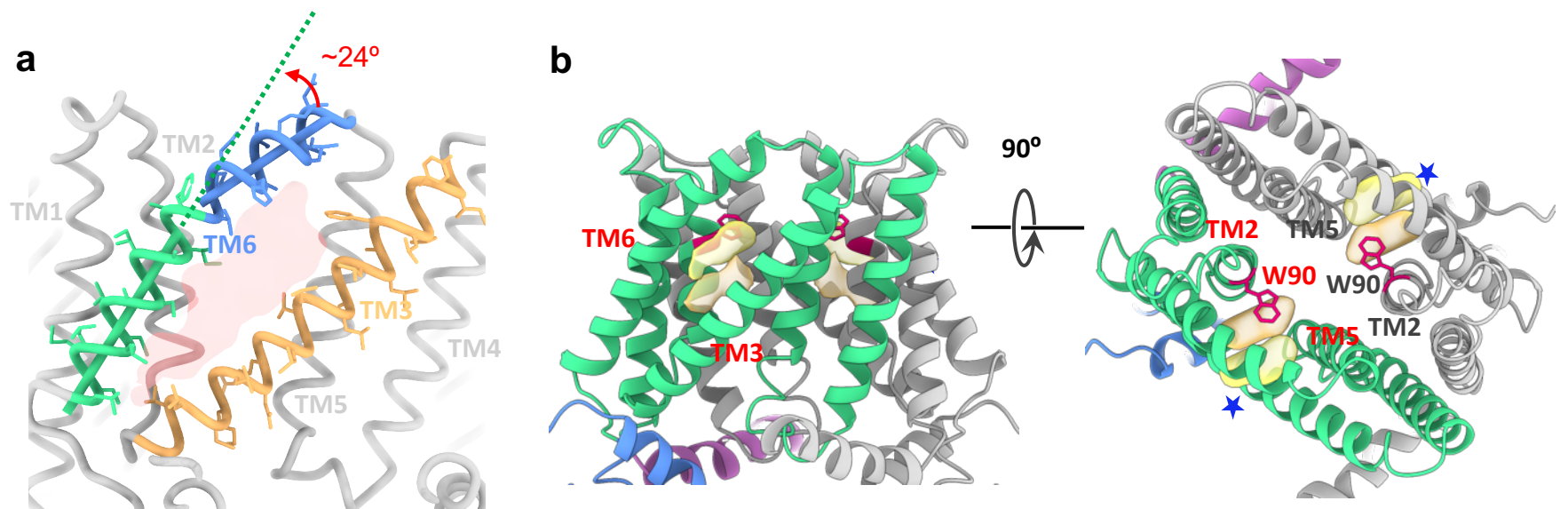
Fig. 4 The lateral fenestration in the QUAC1 channel

a, The lateral fenestration, with a dimension of ~6 Å × 20 Å, is shown in transparent red, which is formed by TM2, TM3, TM5 and TM6 from one protomer. A kink (~24°) in TM6 is indicated.

b, The unidentified densities (in yellow) within the fenestration (indicated by arrows). The side view (right) and top view (left) are shown. The W90 residues are shown as red sticks. The locations of fenestration are indicated with a bule stars in the top view.

Figure 5
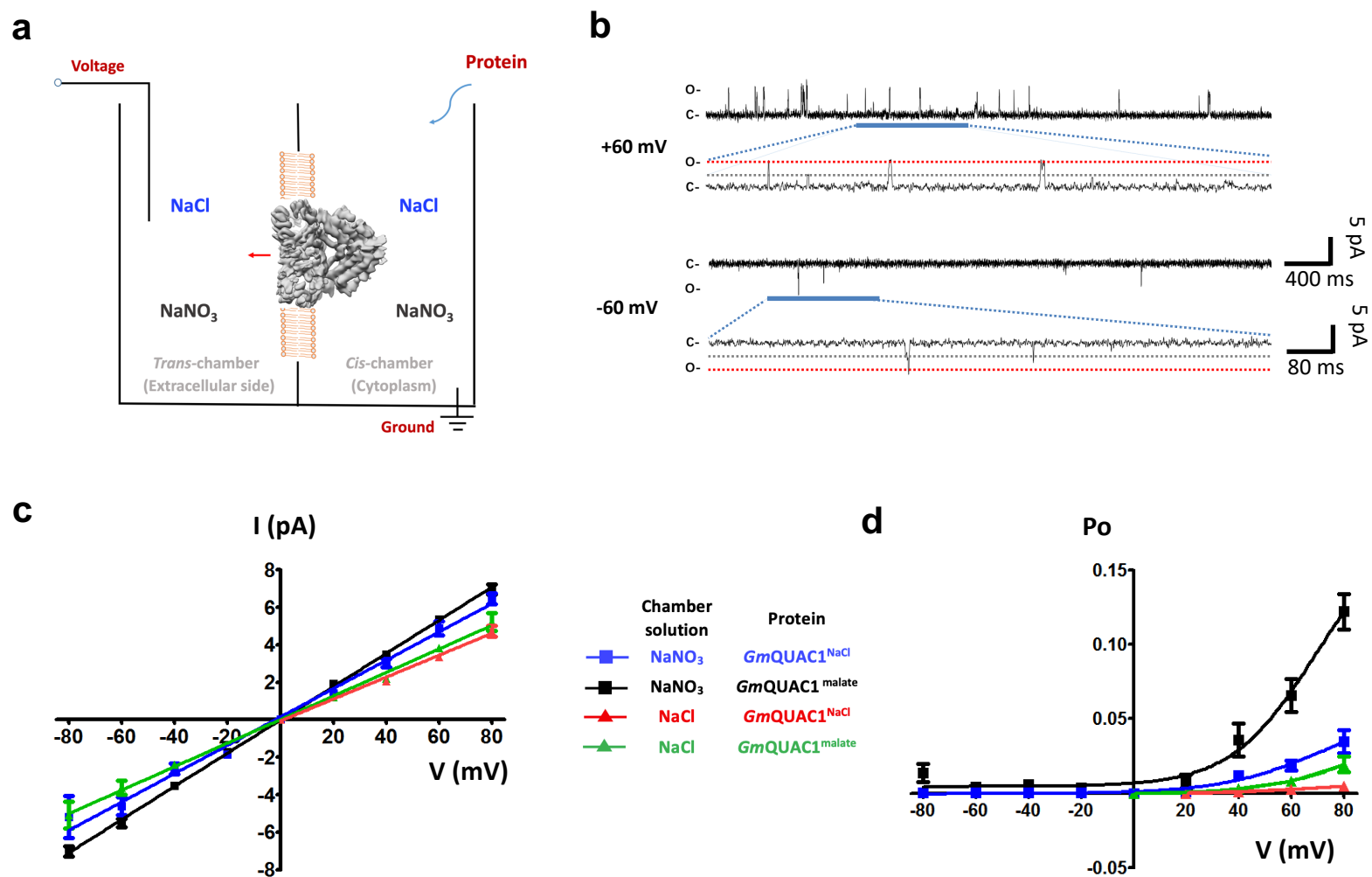
Fig. 5 Single channel analysis of the QUAC1 channel in planar lipid bilayer

a, The schematic illustration of single-channel recording of *Gm*QUAC1 channel in a planar lipid bilayer. The chambers were filled with 1.0 ml of symmetrical solutions of 150 mM NaCl or 150 mM NaNO$_3$, and the *Gm*QUAC1^{NaCl} or *Gm*QUAC1^{malate} (purified in 150 mM NaCl or 75 mM L-malate, respectively) were added to the *cis*-side. The *trans*-chamber, representing the extracellular compartment, was connected to the head stage input of a bilayer voltage-clamp amplifier. The *cis*-chamber, representing the cytoplasmic compartment, was held at virtual ground.

b, Representative current traces for single channel analysis of *Gm*QUAC1^{NaCl} are shown at +60 mV or −60 mV holding potentials in the NaNO$_3$ solution. The closed (C) and full-open (O) states are indicated.

c and d, The current-voltage relationships (**c**) and open probabilities (**d**) for the single-channel recordings of *Gm*QUAC1. The chamber solutions (NaNO$_3$ or NaCl) and protein (*Gm*QUAC1^{NaCl} or *Gm*QUAC1^{malate}) are indicated in the inset (Data are mean ± SEM, n≥4).
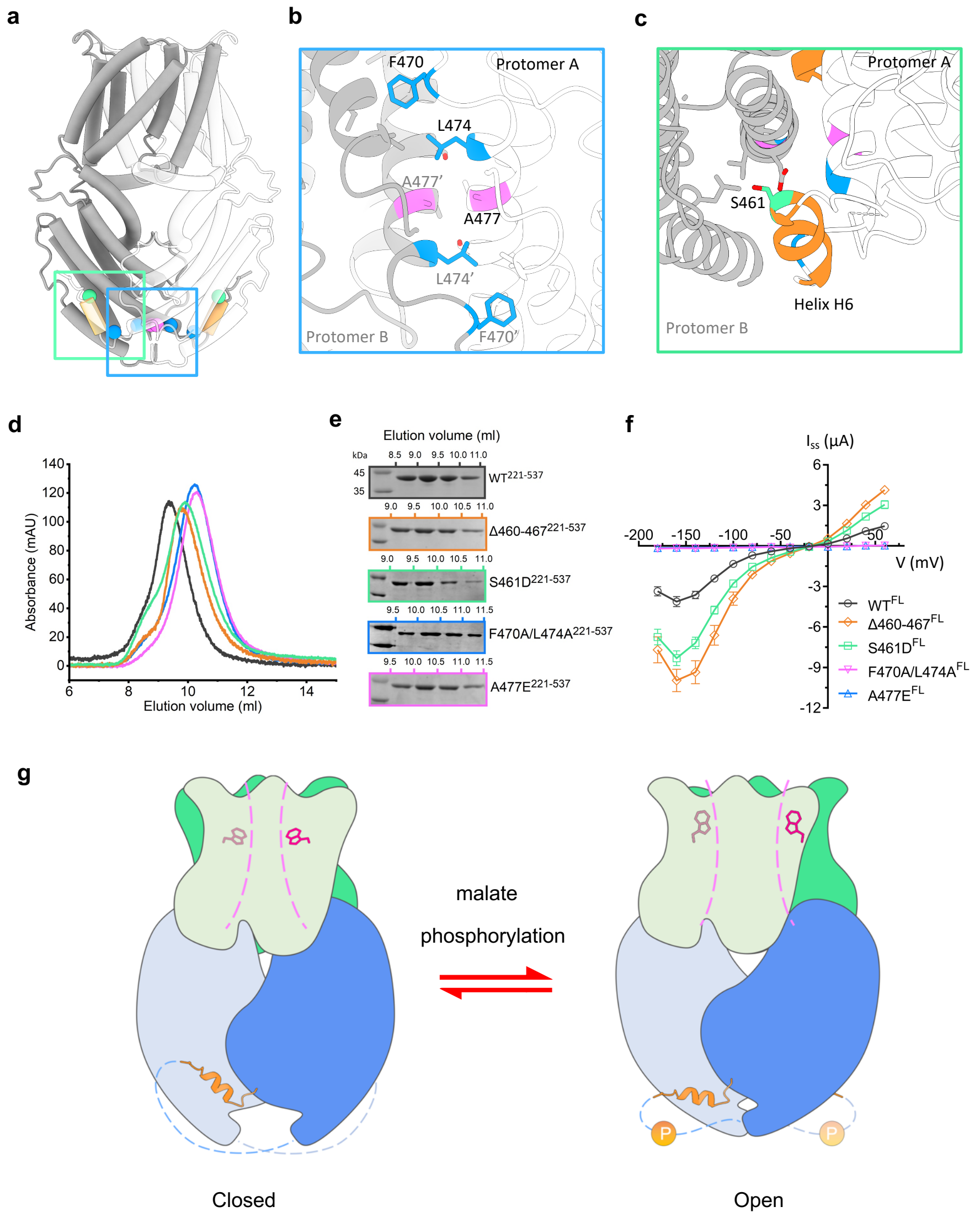
Figure 6

a

b

c

d
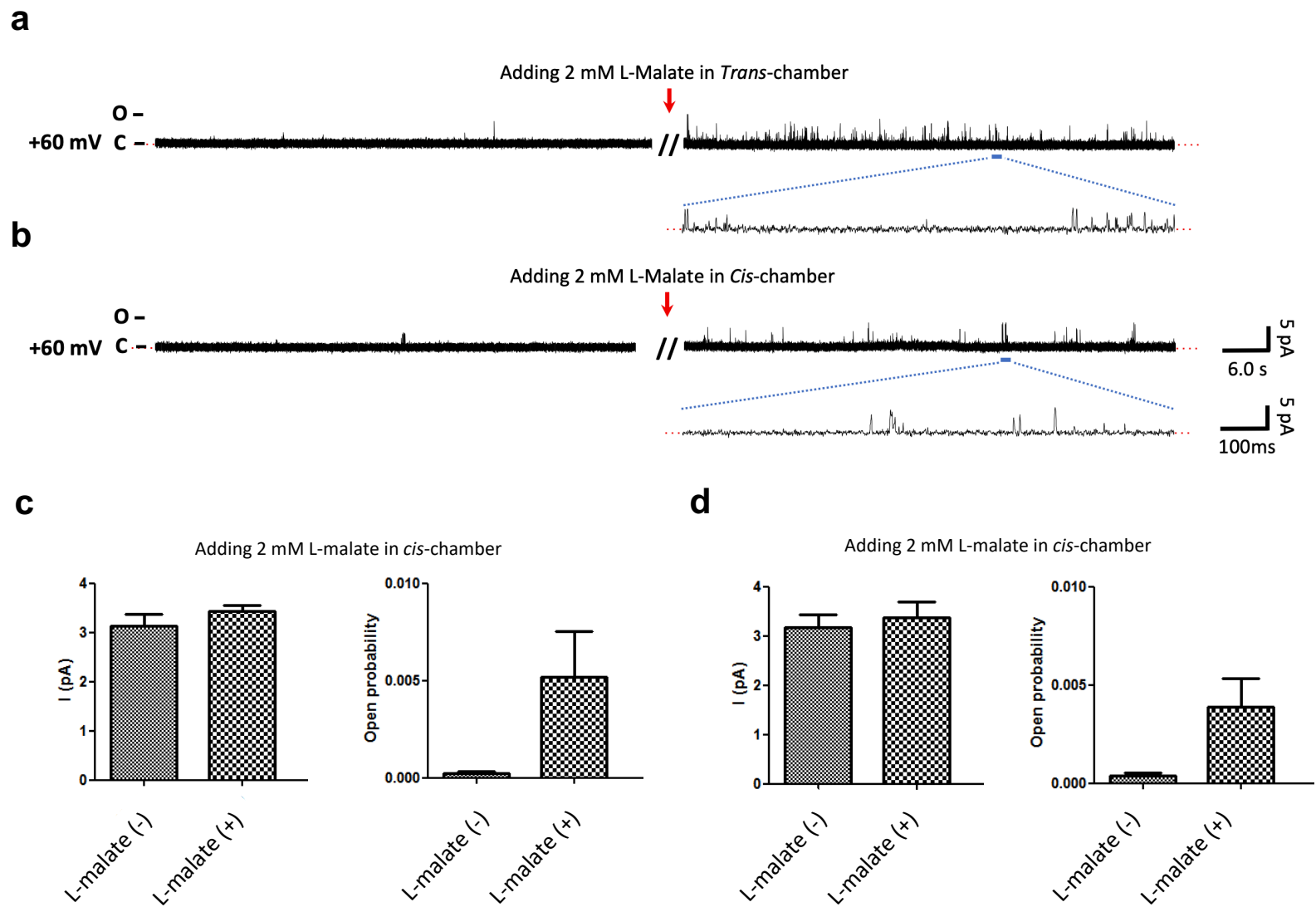
Fig. 6 Single channel analysis of malate regulation on QUAC1

a and **b,** The chambers were filled with symmetrical solutions of 150 mM NaCl, and the purified GmQUAC1^{NaCl} proteins were added to the cis-side. The representative current traces of 60 s at +60 mV, before and after adding 2 mM L-malate to the $trans$- (**a**) or cis- (**b**) chamber, are shown.

c and **d,** The regulation effect of malate on the GmQUAC1^{NaCl} in the NaCl solutions. The current amplitude (left) and open probability (right) analysis for the recordings, before (–) or after (+) addition of 2 mM L-malate to the $trans$- (**c**) or cis- (**d**) chamber (Data are mean ± SEM, n=3 for each group).

Figure 7

a

b

F470

L474

A477'

A477

L474'

Protomer A

Protomer B

F470'

c

Protomer A

S461

Helix H6

Protomer B

d

Absorbance (mAU)

Elution volume (ml)

e

Elution volume (ml)

kDa   8.5   9.0   9.5   10.0 11.0

45
35   WT$^{221-537}$

9.0   9.5   10.0 10.5 11.0

Δ460-467$^{221-537}$

9.0   9.5   10.0 10.5 11.0

S461D$^{221-537}$

9.5   10.0 10.5 11.0 11.5

F470A/L474A$^{221-537}$

9.5   10.0 10.5 11.0 11.5

A477E$^{221-537}$

f

I_{ss} (μA)

V (mV)

- WT^{FL}
- Δ460-467^{FL}
- S461D^{FL}
- F470A/L474A^{FL}
- A477E^{FL}

g

malate

phosphorylation

Closed

Open

Fig. 7 Effect of dimeric interactions on channel activity and the proposed model for QUAC1 regulation

a, The cartoon of the *Gm*QUAC1 channel is shown, with one protomer in grey and one in white. The domain-swapped helix (H6, residues 460-467) is colored in orange, and key residues at the dimeric interface are highlighted: S461 in green, A477 in magenta and F470/L474 in blue.

b and **c,** Close-up views of the cytoplasmic dimer interface. Residues at the dimeric interface are shown as sticks and colored as in (**a**).

d and **e,** The purification of the CHD proteins (residues 221-537, wild-type or mutants) on a Superdex75 (10/300) column. Compared to the wild-type (peak at ~9.2 ml), the eluted peaks for the dimer-disrupting mutants (A477E and F470A/L474A) shift backwards to ~10.2 ml, suggesting a disassociation of dimer into monomer. The elution peaks at ~9.7 ml for the two finger helix altered mutants (Δ460-467 and S461D) suggest loosened conformations upon the removal of finger helix interaction. The eluted fractions were also analyzed by SDS-PAGE, as shown in (**e**).

f, The TEVC recording of *Gm*QUAC1 channel (wild-type and mutants) in *Xenopus laevis* oocytes. The same set of mutations, as in (**d**), were generated into full-length constructs for conductance measurement in the bath solution of 30 mM L-malate (Data are mean ± SEM, n≥8).

g, Model for the QUAC1 channel regulation. Upon malate binding, the QUAC1 undergoes intramolecular domain reorganization to form a twisted bi-layer architecture, and subsequently induces the conformational change of the toggle switch W90. These changes promote the channel conversion from closed to open state. Other modulations, such as phosphorylation or calmodulin binding, can further enhance the malate-mediated activation, probably via the release of its inhibitory domain-swapped helix from the inter-protomer interaction.